Increased laser-accelerated proton energies via direct laser-light-pressure acceleration of electrons in microcone targets

Cite as: Phys. Plasmas **18**, 056710 (2011); https://doi.org/10.1063/1.3575624
Submitted: 20 November 2010 • Accepted: 09 March 2011 • Published Online: 23 May 2011

S. A. Gaillard, T. Kluge, K. A. Flippo, et al.

Increased laser-accelerated proton energies via direct laser-light-pressure acceleration of electrons in microcone targets[a)]

S. A. Gaillard,[1,b)] T. Kluge,[1] K. A. Flippo,[2] M. Bussmann,[1] B. Gall,[3] T. Lockard,[4] M. Geissel,[5] D. T. Offermann,[2] M. Schollmeier,[5] Y. Sentoku,[4] and T. E. Cowan[1]
[1]*Helmholtz-Zentrum Dresden Rossendorf, Institut für Strahlenphysik, PF 51 01 19, Dresden, 01314, Germany*
[2]*Los Alamos National Laboratory, P-24, P.O. Box 1663, MS E526, Los Alamos, New Mexico 87545, USA*
[3]*Electrical and Computer Engineering Department, University of Missouri-Columbia, 227 Engineering Building West, Columbia, Missouri 65211, USA*
[4]*Department of Physics, University of Nevada, Reno, MS 220, 1664 North Virginia St., Reno, Nevada 89557, USA*
[5]*Sandia National Laboratories, P.O. Box 5800, MS 1193, Albuquerque, New Mexico 87185, USA*

(Received 20 November 2010; accepted 9 March 2011; published online 23 May 2011)

We present experimental results showing a laser-accelerated proton beam maximum energy cutoff of 67.5 MeV, with more than 5×10^6 protons per MeV at that energy, using flat-top hollow microcone targets. This result was obtained with a modest laser energy of ~80 J, on the high-contrast Trident laser at Los Alamos National Laboratory. From 2D particle-in-cell simulations, we attribute the source of these enhanced proton energies to direct laser-light-pressure acceleration of electrons along the inner cone wall surface, where the laser light wave accelerates electrons just outside the surface critical density, in a potential well created by a shift of the electrostatic field maximum with respect to that of the magnetic field maximum. Simulations show that for an increasing acceleration length, the continuous loading of electrons into the accelerating phase of the laser field yields an increase in high-energy electrons. © *2011 American Institute of Physics*. [doi:10.1063/1.3575624]

I. INTRODUCTION

Laser-accelerated particle beams,[1] and in particular ion beams,[2–5] are of considerable interest for many applications in science and technology, such as the study of astrophysical phenomena,[6] nuclear reactions and isotope production,[7,8] ion fast ignition,[9] inertial confinement fusion,[10–13] the radiography of dense objects, transient electric and magnetic fields,[14,15] and as an injector for accelerators.[16–18] They also have been proposed for use in medicine, for radiation oncology for proton or ion therapy.[19–21] For the latter application, techniques have been suggested to either use the entire spectral distribution of the proton beam,[22] or to modify the proton spectrum to a quasimonoenergetic narrow-band distribution.[23–27] However, the critical parameter remains being able to maximize the proton cutoff energy.

For an entire decade, using flat-foil targets, or any other target type or geometry, the highest recorded proton energy remained 58 MeV (Fig. 1, green diamond), obtained 10 years ago on the Nova PW laser with 423 J of laser energy.[2] Though equaled at lower laser intensity (Fig. 1, light purple square),[28] it had never been surpassed,[29] despite some of the data being acquired with a significantly higher laser energy of up to 1000 J (Fig. 1, purple triangle)[29] or intensity of up to $\sim 6 \times 10^{20}$ W/cm^2.[30]

In theory and simulations, new mechanisms have been proposed to significantly enhance the ion energy. They include the laser-piston regime,[32,33] the radiation pressure acceleration (RPA) mechanism,[34,35] and the break-out afterburner (BOA) mechanism.[36,37] All of these mechanisms, to be fully realized, have requirements which have, together, not yet been achieved in the laboratory: an ultrahigh contrast (to be able to shoot targets thinner than 100 nm) and very high laser intensities, starting at $\sim 10^{21}$ W/cm^2; and RPA adds a third requirement, e.g., circular polarization.

With the most understood and efficient laser-ion acceleration mechanism demonstrated to date, target normal sheath acceleration (TNSA),[38] one can use different targets geometries, other than flat foils, in order to achieve higher ion energies. Within this TNSA framework, where one usually assumes an isothermal[39] or adiabatic[40] expansion of the plasma into vacuum, increasing the electron temperature (while keeping the hot electron number constant) will increase the maximum ion energies. Target geometries proposed to do so include mass-limited or reduced-mass targets (RMTs),[41–43] stacked foils,[44,45] and cone targets.[46–49] RMTs have recently been shown experimentally[43] to enhance the maximum proton energy due to recirculating electrons, confined in a smaller target volume.

In this paper, we present a more sophisticated target geometry yielding an increase of the resulting maximum proton energy. The source of these enhanced proton energies is attributed, from 2D simulations, to a new mechanism altering the TNSA hot electron population, and is based on direct laser-light-pressure acceleration (DLLPA) of electrons along the cone wall surface in a field confined region (as described in Sec. IV); while the laser-light microfocusing effects in this cone target geometry (i.e., optical collection and guiding), previously discussed in Ref. 49, are alone insufficient to explain the hotter electrons seen in our simulations (as explained in Sec. III).

[a)]Paper NI3 4, Bull. Am. Phys. Soc. **55**, 195 (2010).
[b)]Invited speaker.

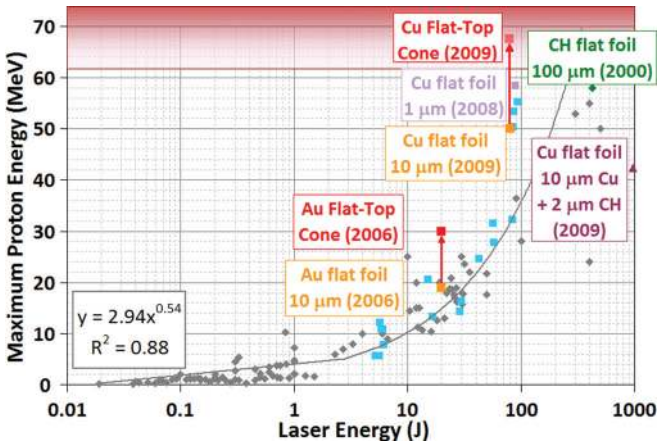

FIG. 1. (Color) Maximum proton cutoff energy (MeV) as a function of laser energy (J) for all published laser systems, with laser intensities from 10^{17} to 6×10^{20} W/cm^2, energies from 19 mJ to 965 J, pulse durations from 30 fs to 10 ps, and reported ASE contrasts from 10^{-5} to $<10^{-9}$, for any type (metal and plastic) and thickness of flat-foil targets, but choosing, for each reported experiment, the highest proton energy (gray diamonds) [see Ref. 29 and references therein]; trend is for all diamonds; the purple triangle represents a shot from the Omega EP laser at 10 ps;[29] all squares are Trident data points; the light purple square represents a shot on a 1 μm Cu flat foil (using a laser contrast of $<10^{-7}$),[28] the red (orange) squares represent shots on Au (Ref. 50) and Cu Flat-Top Cone (flat foil) targets. The green diamond represents the 2000 Nova PW record.[2] The lower red line shows the beginning of the oncological therapeutic window at 62 MeV (depth of 30 mm) for eye cancer,[31] which extends to >200 MeV (depth of 30 cm) for deeply seated tumors.[19]

Our data demonstrates that, using hollow flat-top cone (FTC) targets, at 80 J of laser energy and about 1.5×10^{20} W/cm^2 of averaged laser intensity, proton energies well above 58 MeV can be reproducibly produced. We point out that the laser energy used here is significantly lower than what was being used in previous experiments to achieve ~60 MeV protons (>400 J in Ref. 2 and up to 400 J in Ref. 30). This means that these results are interesting for many applications as the laser energy (J) per ion energy (MeV) can be reduced, for a given laser system. This is especially beneficial for laser systems prospected for tumor therapy that must have sufficiently high repetition-rates, in order to supply the required particle fluxes of 10^{10} particles/s.[19] Using current technology, this necessitates the required laser pulse energy should not exceed hundreds of Joules.

Previously, an increase in maximum proton energy from 19 MeV—using a flat-foil target, to over 30 MeV—using a FTC target had been observed,[50] labeled in Fig. 1 as "Au Flat Foil 10 μm (2006)" and "Au Flat-Top Cone (2006)," respectively. These experiments were performed on the Trident laser at pulse energy of 20 J, with the intrinsic amplified stimulated emission (ASE) contrast of mid 10^{-7} (Fig. 3, blue curve). This increase was attributed mainly to the cone geometry guiding the laser light, and producing hotter electrons, by better laser absorption, due to an increased interaction area and an increased intensity, as in Ref. 49. In that experiment, however, no diagnostic of the hot-electron distribution inside the cone was available. When more energy was available in the laser system, and a higher intensity, due to the addition of a deformable mirror[51] (not available in Ref. 50), a follow-on experiment on Trident using ~80 J at an intrinsic ASE contrast of mid 10^{-7} (Fig. 3, blue curve) was performed, employing target self-emission diagnostics. This did not show an increase in proton energy,[28] and was identified to be due to a large preplasma filling the cone, causing the laser to be absorbed far from the flat top, preventing the efficient transport of hot electrons to the sheath.[28,52] In this article, we describe new experiments performed at 80 J, but at a much higher ASE contrast, better than 10^{-9} (Fig. 3, green curve),[53] which minimized the preformed plasma. As compared to 50 MeV obtained using a flat foil, the proton energies were observed to be significantly enhanced, up to 67.5 MeV, labeled in Fig. 1 as "Cu flat foil 10 μm (2009)" and "Cu Flat-Top Cone (2009)," respectively. Prior simulations focused on the laser interacting with cone targets along the longitudinal axis of symmetry of the cone (coaxially).[49,50] In this work, we systematically study the local interaction of the laser with both the flat top and the cone wall, via simulations using the experimental parameters. These simulations yield a novel understanding of laser-accelerated protons from cone-shaped targets. Our findings should lead to a new path to even higher proton energies in the future, using simpler and better optimized targets.

II. TARGET PERFORMANCE BASED ON X-RAY IMAGING AND PROTON CUTOFF ENERGIES

The experiments were performed at the Los Alamos National Laboratory (LANL) Trident 200 TW chirped-pulse amplified (CPA; Ref. 54) short-pulse laser beam. The experimental setup is illustrated in Fig. 2.

The 670 ± 130 fs, 82 ± 15 J laser pulse with a central wavelength of 1.054 μm interacted normal to the flat top of the Cu FTC target, as shown in Fig. 2. The laser was linearly polarized in the vertical direction [out of the plane in Fig. 2(a)] and, therefore, the laser interaction at normal incidence with the FTC flat top was S-polarized, while the laser interaction with the cone walls in the vertical plane was P-polarized, as illustrated by the laser E-field shown in Fig. 6(a) (inset, E_L, purple arrow). The laser was focused at the plane of the FTC top to a 7 μm full width at half maximum (FWHM) spot, containing 47% of the energy for an average laser intensity of $1.5(\pm 0.5) \times 10^{20}$ W/cm^2. The laser was generally aligned down the throat of the cone using a backscatter focal diagnostic imaging technique.[55] The aligning and pointing accuracy is usually better than 10–15 μm; but in some cases, it can be occasionally up to ~100 μm, due to uncontrolled vibrations in equipment neighboring or within the laser facility.

The laser contrast was 10^{-9} (which corresponds to the detection limit of the third order cross-correlator) or better at 80 ps before the main pulse, and 10^{-6} 20 ps before the main pulse (Fig. 3, green curve).

To study the effect of different target geometries on proton energy, we compared flat-foil targets to a variety of FTC targets and RMTs of various diameters. The FTC targets of the experimental campaign had a variety of top and neck diameters: the top diameters ranged from ~90 to 325 μm, and the neck diameters ranged from a neck outer diameter (OD) of ~10 to ~160 μm, and a neck inside diameter (ID) of a few microns to ~140 μm (see Fig. 4).

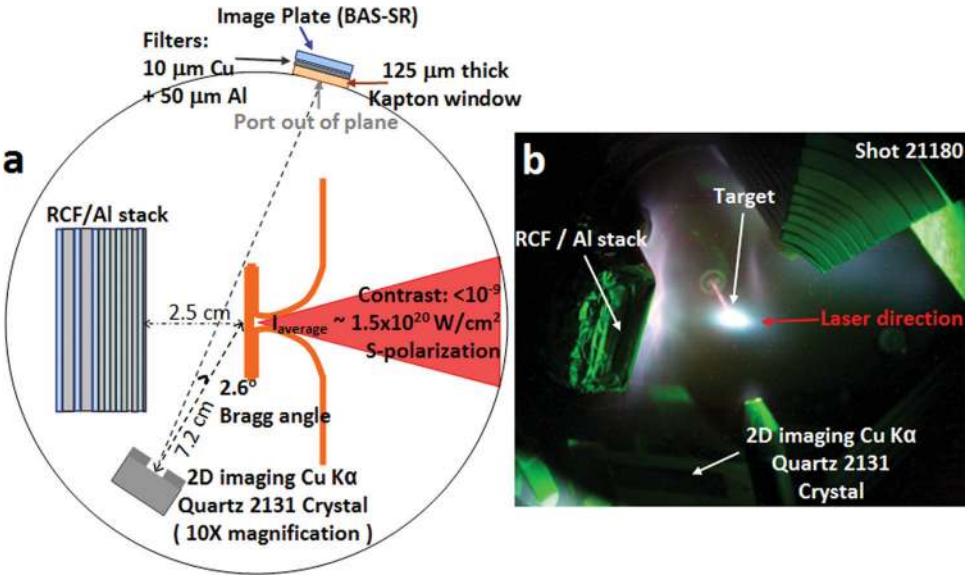

FIG. 2. (Color) (a) Schematics of the experimental set-up (top view): the incident laser (red triangle) propagates down the throat of the hollow flat-top cone and interacts with the flat top; protons are recorded in the Radiochromic film stack, and 2D Cu Kα x-rays images are formed on a spherical 2131 quartz crystal and recorded by an image plate; (b) Picture of the inside of the target chamber, taken during a shot, and integrated over 5 s.

The hot electron production and transport in the target were diagnosed using Cu Kα x-ray emission[57] of the FTC targets from a 2D spherical quartz 2131 crystal imager, with a 10 μm resolution, combined with an image plate (BAS-SR; Ref. 58) detector and a set of filters (Al, Kapton and Cu). From this diagnostic, one could then infer where the laser was primarily being absorbed into hot electrons.[52] The amount of Cu Kα emission is related to the local energy density distribution of a portion of the hot electrons above 8 keV. As illustrated in Fig. 5, the Cu Kα x-ray emission characteristics of each target depend on where the emission takes place: for an FTC the important emission zones are the top (TE), the cone walls (CWE), and the supporting foil (SFE). Integrating the Cu Kα yield over these cone areas (see Fig. 5, legend), for each target, yields the characteristic ratio ε [i.e., top emission over total emission, $\varepsilon = \mathrm{TE}/(\mathrm{TE} + \mathrm{CWE} + \mathrm{SFE})$].

Simultaneously, the laser-accelerated protons were recorded in RadioChromic Film (RCF; Ref. 59) stacks, placed 2.5 ± 0.5 cm behind the target, and analyzed via RadioChromic Film Imaging spectroscopy (RIS; Ref. 60). The RCF combined with the x-ray imager allowed us to correlate proton energies to the laser-cone emission, and to understand the electron transport in the target. The two best performers in terms of proton energy were two FTCs (named Γ1 and Γ2) with very dissimilar geometries, the characteristics and performances of which are summarized in Table I. In fact, no correlation between proton energy was found with cone geometry, i.e., neck diameter, top diameter, nor top-to-neck diameter ratio, unlike in Ref. 50, where a ratio of 4 was found to be optimal. However, in this work, a correlation was found between proton energy and x-ray emission regions in the FTCs, regardless of cone geometry.

Looking at the Cu Kα emission regions, as shown in Fig. 6, we find that Γ1 and Γ2 exhibit strong TE as well as CWE [Fig. 6(b), green line-outs]. Two more groups are isolated in Fig. 6: one exhibiting much more TE [Fig. 6(b), red line-out], and the other much more CWE and/or SFE [Fig. 6(b), blue line-outs]. When the ratio of these emission regions are taken, as described above, we find that all the shots fall into four distinct groups labeled Σ, Γ, Ψ, and Φ, depending on the value of ε, for ε centered at 0.25, 0.5, 0.75, and 1, respectively (Fig. 7). Together, Figs. 6–8 summarize the principal experimental results. These include: the Cu Kα x-ray images from selected targets: Σ1, Γ1, Γ2, Ψ1, and Ψ2 [Fig. 6(a)]; the Cu Kα x-ray integrated and averaged lineouts from selected targets: Σ1, Γ1, Γ2, and Ψ1 [Fig. 6(b)]; a summary of the maximum proton energy observed for each shot, grouped as a function of ε (Fig. 7), and as a function of laser energy (Fig. 8).

We find that the efficacy of the proton acceleration with respect to maximum energy correlates well with ε (Fig. 7).

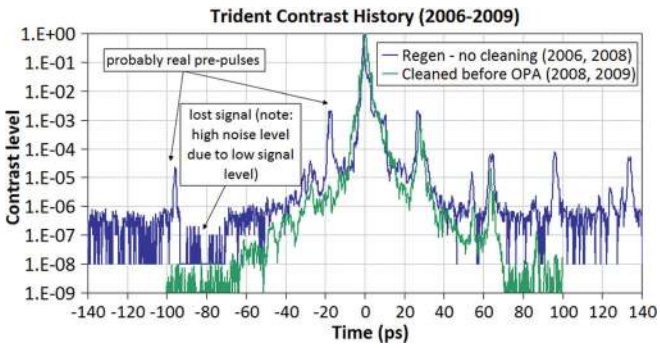

FIG. 3. (Color) Trident laser's third order cross-correlation contrast curves:[56] (blue) intrinsic contrast (mid 10^{-7} 140 ps before the main pulse, 10^{-7} 80 ps before the main pulse, and 10^{-5} 20 ps before the main pulse); and (green) enhanced contrast (better than 10^{-9} 80 ps before the main pulse, and 10^{-6} 20 ps before the main pulse).

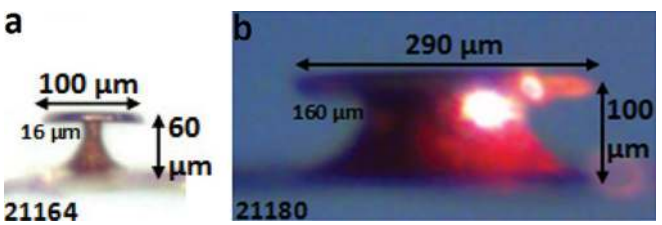

FIG. 4. (Color) Target pictures (to scale): the OD of the various necks ranged from (a) 11 μm (shot 21164) to (b) 160 μm (shot 21180).

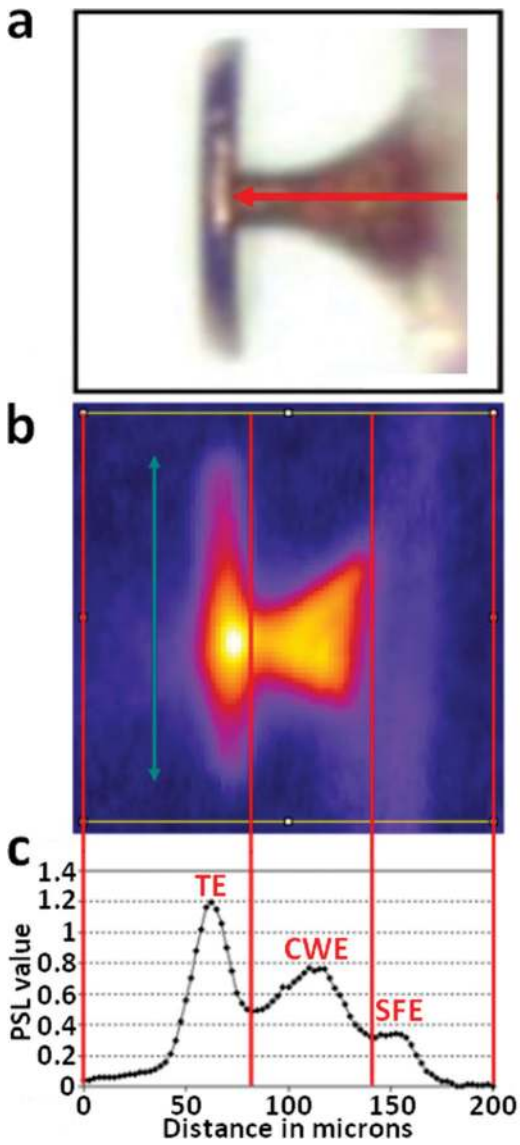

FIG. 5. (Color) Definition of the various Cu Kα emission areas: (a) Picture of an FTC target—the red arrow indicates the laser direction, focused on the inner flat-top surface; (b) Cu Kα image (shot 21169) with the top diameter indicated by the green arrow; (c) Integrated and averaged lineout across the Cu Kα image, showing three distinctive areas, referred to as top emission (TE), cone wall emission (CWE), and supporting foil emission; since all the targets are of different sizes, the height of the box is chosen to be 0.25 times larger than the flat-top diameter.

The highest observed proton energies of 67.5 ± 2.0 and 66.7 ± 2.0 MeV (with the corresponding proton energy spectra Γ1 and Γ2, respectively, see Fig. 10) are in group Γ, which corresponds to the laser interacting significantly with both the cone wall and the flat top, based on the x-ray images [Fig. 6(a)], since the emissions from the top and the cone walls nearly balance. For comparison, similarly thick flat-foil targets yield a maximum proton energy of 50.0 ± 1.5 MeV (i.e., group Φ) under the same conditions. Contrary to our prior expectation[49,50] that the maximum proton energy would arise from a coaxially aligned FTC, where most of the x-ray emission should come from the top (i.e., group Ψ), the experimental results show that, in terms of maximum proton energies, group Ψ is similar to group Φ, i.e., no better than a flat foil; the maximum proton energy in group Ψ was 54.8 ± 1.6 MeV (with the corresponding proton energy spectrum Ψ1, see Fig. 10). Group Φ contains the flat-foil targets as well as the RMTs, one of which had the optimal diameter for this contrast (230 μm), yielding a respectable 59.3 MeV.

TABLE I. Targets Γ1 and Γ2: characteristics (neck OD, top diameter, top thickness, wall thickness, height) and performances (laser-to-proton conversion efficiency for protons above 4 MeV, proton cutoff energy, and number of protons per MeV at the cutoff energy).

	Γ1	Γ2
Neck OD	160 μm	22 μm
Top diameter	290 μm	110 μm
Top thickness	12.5 ± 2.5 μm	12.5 ± 2.5 μm
Wall thickness	10 ± 2.5 μm	10 ± 2.5 μm
Height	100 μm	65 μm
Laser-to-proton conversion efficieny (>4 MeV)	1.75%	1.55%
Proton cutoff energy	67.5 ± 2.0 MeV	66.7 ± 2.0 MeV
Proton number at the cutoff energy	7.00 E + 06	9.00 E + 06

Much of the scatter in the maximum proton energy data of each group in Fig. 7 can be attributed to the variation of the laser pulse energies, as shown in Fig. 8, which indicates that the Γ interaction group outperforms the top-only group Ψ on most shots, as well as the RMT and flat-foil group Φ. Some of the remaining scatter can be traced to variations in the laser intensity, the degree of interaction asymmetry, the presence of SFE (Fig. 8, black cross in green, red, and blue squares) and the reduction of the supporting foil size (Fig. 8, red and green circles around the red and green squares, respectively).

It is important to note that, in group Γ, the highest proton energies occur for asymmetric cone wall emissions (i.e., one opposing side wall emits more than the other). This is illustrated by the Cu Kα images in Fig. 6(a) of Γ1 and Γ2, and more clearly through their line-outs in Fig. 9. The asymmetry in Γ2 is less evident than that in Γ1 due to the much smaller neck size and the resolution of the diagnostic.

It is also interesting to note that the best performing target of the top-emission group, Ψ1 (Fig. 8, red square, black border), shows a small asymmetry in the x-ray emission in Fig. 6(a), indicating a slight vertical offset of the incident laser pulse. With the exception of one FTC, all FTC shots above the flat-foil average (dashed black line, Fig. 7) exhibit an asymmetric emission, which is taken as evidence that a P-polarized laser–cone-wall interaction is favorable. On the other hand, the worst FTC performer in group Γ (Fig. 8, green square, black border with cross inside) exhibited a very symmetric cone wall emission, possibly indicating that the laser interaction was offset toward the facing/opposing wall, where the resulting S-polarization would not be optimal for DLLPA (as described below).

In addition to the sources of scatter described above, there is a detector uncertainty in the maximum proton energy measurements of ∼±3% that can be attributed to the variation in the RCF thickness. The laser-to-proton conversion efficiency (for protons >4 MeV) is very similar for FTC

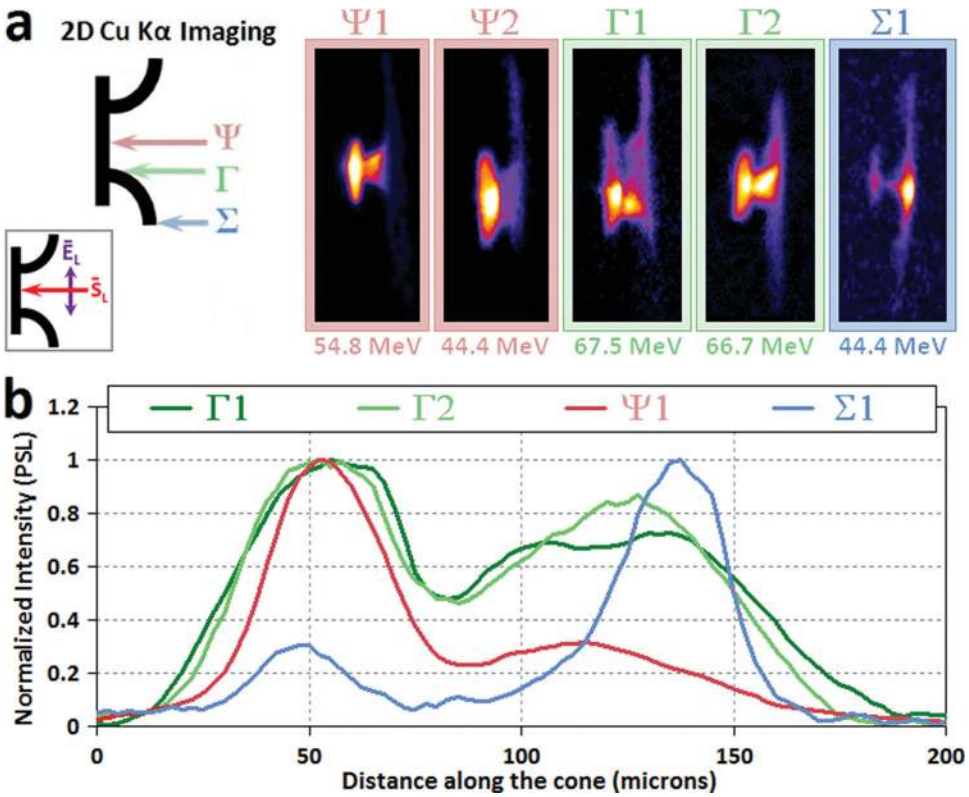

FIG. 6. (Color) Experimental data grouped according to the Cu Kα x-ray emission into three groups for FTCs. Group Ψ shows prevailing emission from the top. Group Γ shows a balanced emission from the top and the cone walls. Group Σ corresponds to the case where the emission is almost all from the cone walls or the supporting foil, due to the laser directly hitting there, and not reaching the flat top. (a, left) The colored arrows for groups Ψ (light red), Γ (light green), and Σ (light blue) indicate approximately how the laser interacted with the FTC targets belonging to each group; (right) Cu Kα 2D imaging (color scale indicating emission intensity, qualitatively) of the FTC targets with the highest proton energy performers of these groups; (inset) The laser polarization is indicated by the purple arrow and vector $\mathbf{E_L}$, while the laser Poynting vector is indicated by the red arrow and vector $\mathbf{S_L}$. (b) Normalized Cu Kα intensity as a function of distance along the longitudinal direction of the FTC for four selected shots (Σ1, Γ1, Γ2, and Ψ1).

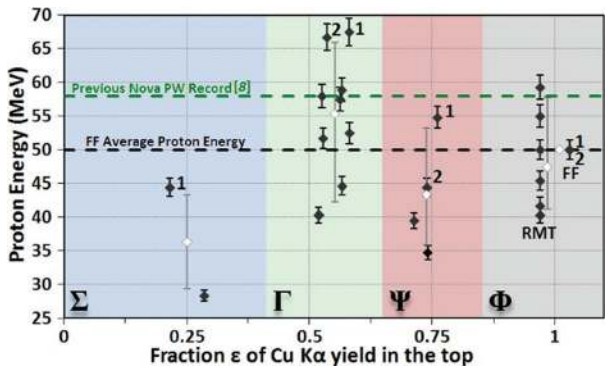

FIG. 7. (Color) Experimental data grouped with respect to maximum proton energy and Cu Kα x-ray emission ratio ε into three groups for FTCs (Σ, Γ, and Ψ) and one for flat-foils and RMTs (Φ); each data point is represented by a black diamond, along with the associated ±3% error bars, and the averaged group value by gray white filled diamonds with 2σ gray error bars.

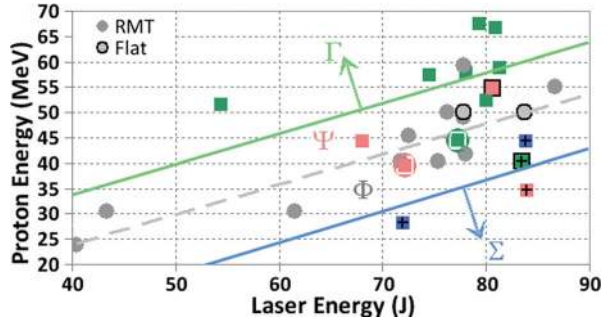

FIG. 8. (Color) Maximum proton cutoff energy for all targets of the entire campaign as a function of laser energy showing relative group performance (delineated by the three colored lines); data points with borders or crosses are explained in the text.

targets (i.e., 1.4 ± 0.4%) and flat-foil targets (i.e., 1.25%), unlike what was reported in Ref. 50 at 20 J of laser energy, where the conversion efficiency (for protons >4 MeV) increased almost 5-fold, from 0.4% for the flat-foil target to 1.9% for the FTC target.

In summary, 2D Cu Kα imaging [Figs. 6(a) and 9] shows that target Γ1, with an extremely large neck of 160 μm OD, yielded the highest proton energy, and also exhibited an asymmetric cone wall emission: the laser interacts with the cone wall while still interacting directly with the flat top. If the laser partially interacts with the cone wall, any oblique reflection from the cone wall could end up increasing the intensity on the flat top. Note that if the laser was centered with respect to the neck (coaxially), for such a wide-neck cone (i.e., 25 times the laser focal spot FWHM diameter), no optical collection or guiding would be expected.[49] Even though target Γ2 had a much thinner neck than target Γ1, with an

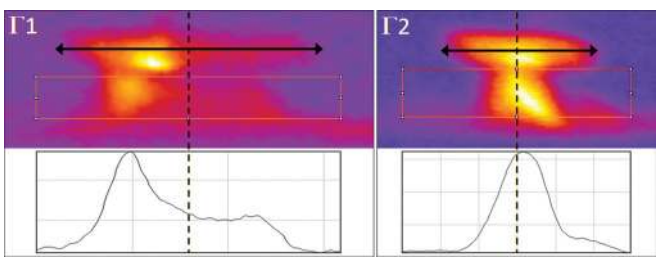

FIG. 9. (Color) (top) Cu Kα images of targets Γ1 and Γ2: the orange rectangles extend across the cone wall region of the FTC, the black arrows show the extent of the fat top, and the vertical dotted lines show the longitudinal axis of symmetry of the FTCs; (bottom) Integrated line-outs of the cone wall region delimited by the rectangle, showing the asymmetry of the emission in the cone wall region.

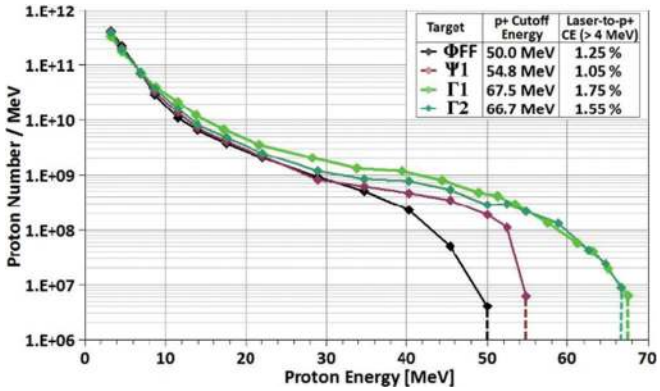

FIG. 10. (Color) Experimental proton spectra for a flat foil, ΦFF, and FTCs Ψ1, Γ1, and Γ2; (inset) Detector cut-off energies (denoted by the dashed vertical lines) and laser-to-proton conversion efficiency (CE) using a simple binned average of the data.

OD of ~22 μm, resulting in an inner diameter of the order of the laser focal spot size, it did not perform better than target Γ1, unlike what would be expected in a pure microfocusing case, but yielded the second highest proton energy. The interaction with the cone wall was in this case also asymmetric, as determined from 2D Cu Kα [Figs. 6(a) and 9]. Therefore, the important findings are that the neck diameter is not a crucial parameter, but rather that it is when the laser interacts with both the cone wall and the flat top that an enhancement in proton energy is obtained. Moreover, the size of the flat top is not observed to be a dominant parameter.

In retrospect, these new findings are not in contradiction with previous observations,[50] which showed that, although the target yielding the highest proton energy (>30 MeV) at 20 J had a 25 μm OD neck and a flat top of 100 μm, some good performers with respect to maximum proton energy had much wider necks (up to 90 μm OD) and much larger tops (up to 270 μm). Unfortunately, the degree of grazing in any of those cones is unknown, due to the absence of a 2D x-ray imaging diagnostic in the experiments reported in Ref. 50.

III. SIMULATIONS: EXTENDING THE EXPERIMENTAL RESULTS

In order to identify the relevant mechanisms leading to the observed high proton energies, a series of 2D particle-in-cell (PIC) simulations using the collisional code PICLS (Ref. 61) were conducted, the results of which are presented in Figs. 11 and 12.

A 0.5 μm scale-length preplasma was added inside the cone walls to mimic the effect of the small remaining laser prepulse. Ionization and collisions[61] were included. The target electron density, when fully ionized, was set to 40 n_c, as compared to that of real copper (~2000 n_c). This reduction in electron density helps decrease the computational costs, to allow for a complete parameter study; but as it is still well above the critical density, the simulations still show the important physics. An area of 600×250 μm^2 (divided into 14880 cells × 6200 cells), using 54 macroparticles/cell and 1911 electrons/macroparticle, and with a temporal resolution of $\tau/24.8$, where τ is one laser oscillation period, was simulated ($\tau =$ 1 μm/c, where c is the speed of light). The simulations were stopped after 1.7 ps, at which point in time it was verified that the protons had reached more than 98% of their final energy. The simulated laser parameters closely matched the experimental parameters. The laser intensity was set to 2×10^{20} W/cm^2, rising with a half-Gaussian profile ($\sigma =$ 20τ), staying constant for 128τ (flat-top pulse), and finally dropping with a symmetric half-Gaussian profile. The laser was focused to a spot size diameter of 6 μm FWHM, inside the FTC, on the flat top, and was incident normal to the plane of the flat top. The focal plane was the same in the experiments and in the simulations [see Fig. 6(a), for example].

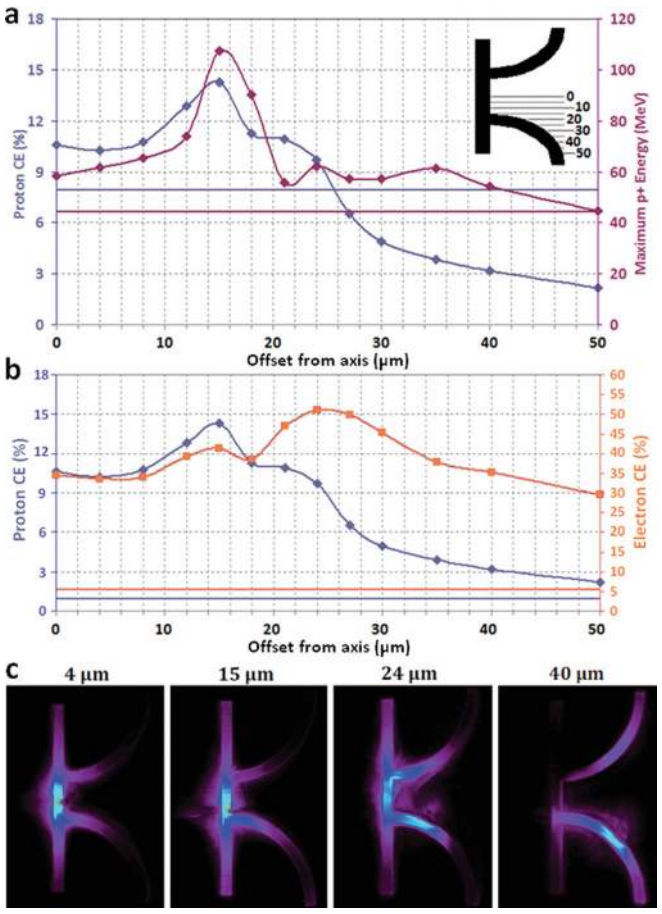

FIG. 11. (Color) (a,b) PICLS simulations at t = 1643 fs: As a function of laser offset (horizontal lines indicate the RMT cases), (a) proton energy (right, maroon) and laser-to-proton conversion efficiency for all proton energies (left, blue) and (b) laser-to-electron conversion efficiency for all electron energies (right, orange) and laser-to-proton conversion efficiency for all proton energies (left, blue); the simulated maximum proton energy of 44 MeV for RMTs is very close to the average experimental value of 47 MeV; (a, inset) FTC geometry (FTC1) and offset distances in μm. (c) PICLS simulations at t = 1026 fs of the electron energy density in the FTC target for three different offsets: 4, 15 (grazing), 24, and 40 μm; the laser is incident in the cone as illustrated in the inset in (a); logarithmic rainbow color scale normalized to respective maximum.

These simulations investigated the effect of the neck diameter, as well as that of the laser offset for a given neck diameter. Table II gives the geometric details of the targets used in the simulations: FTC1 has dimensions in-between those of targets Γ1 and Γ2 [Fig. 4(a)] and a 30 μm ID, while FTC2 has a 1 μm ID. All targets were made of copper, and the flat top was covered with a 2 μm proton layer (red layer, Table II).

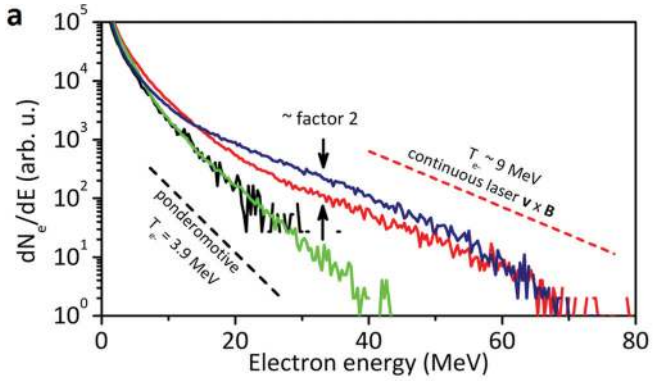

b

	RMT	FTC1 no offset	FTC1 15 μm offset	FTC2 no offset
CE (>0 MeV)	8%	11%	14%	17%
CE (>4 MeV)	7%	9%	12%	16%
Emax_p+	44 MeV	58 MeV	107 MeV	111 MeV

FIG. 12. (Color) PICLS simulations at $t = 900$ fs for different target geometries (RMT, FTC1, and FTC2) and laser offsets (0 and 15 μm): (a) Number of electrons as a function of electron energy (MeV); (b) Table summarizing the laser-to-proton conversion efficiencies (%), for all proton energies (CE > 0 MeV) and for proton energies above 4 MeV (CE > 4 MeV), for comparison with experiments; and the maximum proton cutoff energies (MeV).

Figure 11(a) shows, as a function of the laser offset with respect to the center axis of FTC1 [Fig. 11(a), inset], the maximum proton cutoff energy (maroon curve, right axis), and the laser-to-proton conversion efficiency for all proton energies (blue curve, left axis). Starting from small offset values [e.g., Fig. 11(c), 4 μm], the maximum proton energy increases until it reaches a maximum (107 MeV), which is more than twice the energy seen from an RMT (44 MeV, maroon horizontal line). This optimum is reached for an offset of 15 μm, where the laser axis is tangential to the cone wall [i.e., grazing along the cone wall, Fig. 11(c), 15 μm]. For greater offsets [e.g., Fig. 11(c), 24 and 40 μm], the maximum proton energy approaches that of an RMT. The conversion efficiency is maximized (14%) when the proton energy is the highest, i.e., for a 15 μm offset. For large offsets (i.e., >25 μm), it drops below the RMT energy level (8%, blue horizontal line), due to the fact that the laser is deflected by the cone wall backward and does not focus on the flat top. This latter case corresponds to the FTCs in group Σ, for which the laser was misaligned and did not reach the top.

As shown in Fig. 11(b), the laser-to-electron conversion efficiencies for all electron energies (orange curve, right axis) correlate well with the laser-to-proton conversion efficiencies (blue curve, left axis): they both exhibit a maximum for the 15 μm offset, and fall off for both smaller and larger offsets. However, the laser-to-electron conversion efficiency exhibits a secondary, larger maximum, at a specific larger offset of 24 μm which arises when a portion of the laser light is reflected to the opposite corner of the cone top, creating a second hot electron source [Fig. 11(c)]. In this case, the laser-to-electron conversion efficiency increase does not translate into more energy for the TNSA protons, since the electrons from the first wall interaction are not efficiently transported to the cone tip and therefore do not contribute to the creation of the relevant sheath.

Figure 12(a) shows the electron spectra of the simulated targets with no laser offset, i.e., RMT (black), FTC1 (green) and FTC2 (blue), and FTC1 with a 15 μm laser offset (red); the table in Fig. 12(b) summarizes the corresponding laser-to-proton conversion efficiencies [for protons with energy above 0 MeV (CE > 0 MeV), and above 4 MeV (CE > 4 MeV)] and maximum proton cutoff energies. The electron spectra of the RMT and of the FTC1 with no offset are similar with respect to temperature and density. Consequently, only a small increase in proton energy (from 44 to 58 MeV) and conversion efficiency for all proton energies (from 8% to 11%) is seen. In the case of grazing incidence, when the laser interacts strongly with both the flat top and the cone wall of FTC1 (15 μm offset), the electron spectrum shows a much higher hot-electron number, maximum cutoff energy, and temperature. Hence, the strong increase in proton energy from 58 to 107 MeV (and a comparatively small increase in conversion efficiency for all proton energies from 11% to 14%) is accompanied by the appearance of a high-temperature, high-energy component in the electron population. By reducing the cone neck ID from 30 to 1 μm (FTC2), the laser can now interact with both cone walls and the flat top; therefore, the conversion efficiency for all proton energies increases from 14% to 17%, and the total hot-electron number is doubled in the [~20 MeV; ~40 MeV] energy range; however, almost no increase in proton energy is observed.

From previous simulations,[49] it is expected that the microfocusing of the laser pulse in the cone geometry enhances the electron number and energy at the tip of the cone, which should be the same in our case. As the effective focused laser intensity becomes greater, the resulting increase in the laser strength parameter a_0 should also yield a higher electron temperature, which can be estimated using the ponderomotive scaling in Ref. 38, i.e.,

$$T_{e,\mathrm{pond}} = 0.511\left(\sqrt{1+\frac{a_0^2}{2}}-1\right), \tag{1}$$

At a laser intensity of 2×10^{20} W/cm^2 ($a_0 = 12$), using Eq. (1), one finds the ponderomotive temperature to be $T_{e,\mathrm{pond}} = 3.9$ MeV. As found in the simulations, the electron temperature for both the RMT (black) and the FTC1 with no laser offset (green) is $T_{e,\mathrm{PICLS}} = 4.4$ MeV [Fig. 12(a)], which is consistent with the ponderomotive scaling for the a_0 of 13.3 measured in the simulations. In the simulation case of FTC1 with grazing laser incidence (red), the electron temperature is increased to $T_{e,\mathrm{PICLS}} = 9.2$ MeV. This increase

TABLE II. Geometry of the targets used in the simulations.

Target denomination	FTC1	FTC2	RMT
Target schematics			
Cone wall curvature radius (μm)	80	80	—
Top diameter (μm)	180	180	180
Wall thickness (μm)	10	10	10
Neck ID (μm)	30	1	—

can only be partially attributed to the effective intensity increase resulting from microfocusing. The microfocused intensity in the simulations was measured to be $a_0 = 18.6$, which only corresponds to a $T_{e,pond}$ of 6.2 MeV from Eq. (1). Thus, the local increase in laser intensity seen in the simulations only explains less than 40% (1.8 MeV) of the observed 4.8 MeV electron temperature increase. Furthermore, even though the much thinner necked cone FTC2 (blue) yields more laser microfocusing ($a_0 = 21$), it too yields similar electron temperatures and proton energies (see Fig. 12), which still cannot be explained by the intensity increase alone. This means that the optical collection and guiding mechanism alone is not sufficient to explain—nor correlates with—the considerably higher electron temperatures observed in the simulations. Rather, we find that the high-energy electrons could be generated via DLLPA of surface-confined electrons, as described below.

IV. THE DIRECT LASER-LIGHT-PRESSURE ACCELERATION MECHANISM

For a given angle θ, between the surface normal and the propagation direction of the incident laser light, the interference of the reflected with the incident laser light produces a traveling electric field along the surface with a period of $\lambda_L/\sin\theta$, and a phase velocity along the cone wall of $v_w = c/\sin\theta$, where c is the speed of light. This electric field extracts electrons lying within a skin depth beyond the critical density, in such a way that the resultant electron bunches are separated by approximately $\lambda_L/\sin\theta$, which, for near grazing incidence is about the laser wavelength $\lambda_L = 1$ μm (Fig. 13, top), and not by $\lambda_L/2$ as would be expected from ponderomotive $\mathbf{v} \times \mathbf{B}$ acceleration. Once pulled out of the target, the electrons are confined in a potential well caused by the magnetic field B_z, which is created by the return current inside the cone wall J_x and balanced by the electrostatic field E_y created by the extracted escaping electrons (Fig. 13). A similar effect of magnetic deflection in a self-generated magnetic field has been described in Refs. 49, 62, and 63, and the model developed there can be applied to our target geometry and physical conditions.

Figure 13 (left) shows the magnetostatic and electrostatic fields along a vertical lineout through the cone wall, displaying a shift in the electrostatic field maximum with respect to that of the magnetic field maximum. This shift results in a potential well for the electrons, along the inner cone wall, and in the direction of the laser. In order to discover the origin of the high-energy electrons, Fig. 13 contrasts the spatial distribution of the high, >20 MeV, energy electrons (blue) with that of the low, <20 MeV, energy electrons (red). The high-energy electrons are localized just outside the surface critical density in the potential well. Their density being in phase with the laser electric and magnetic fields, they are bunched at a distance of 1 μm, as shown in the phase-space x-p_y of the high-energy electrons (Fig. 13, top). The number of hot electrons extracted from the surface, per wavelength, is of the order $N_e \sim (a_0 n_c \lambda_L/\pi)\sin\theta$, which is derived in Ref. 64 from the balance equation between the surface field and the electrostatic potential. As predicted,

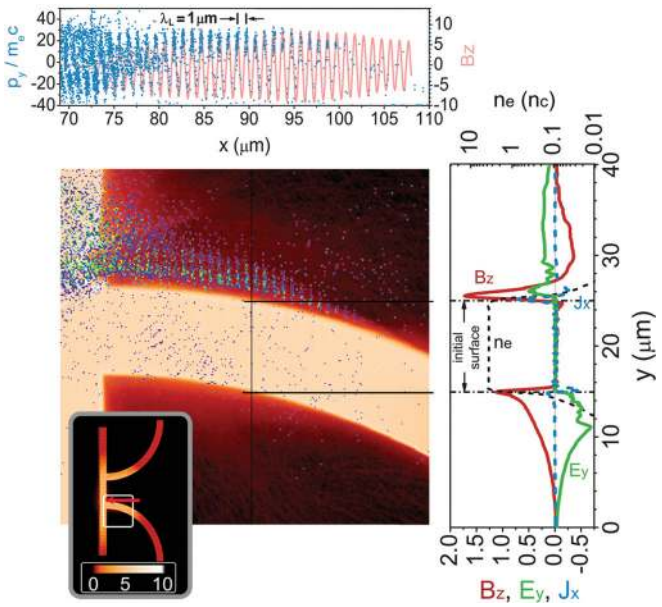

FIG. 13. (Color) Direct acceleration of surface confined electrons by the laser-light-pressure (PICLS simulations): (inset, bottom left) Electron density normalized to n_c; the laser is represented by the red arrow. The central image corresponds to the white box in the inset and shows the electron density and the distribution of the hot electrons ($E_{kin} > 20$ MeV, blue) in bunches separated by 1 μm, trapped outside the target wall in the potential well created by magnetostatic B_z and electrostatic E_y fields (normalized to $E_0 = B_0 c = 2\pi mc^2/\lambda_L e$), self-generated by the escaping electrons and balanced by the surface electron return currents J_x (right). (top) Transverse phase-space of the hot electrons together with the laser B-field.

more hot electrons are extracted and trapped in the simulation as θ approaches $\pi/2$ (i.e., near grazing incidence, $x > 90$ μm). If the initial velocity is close to the phase velocity of the laser light—that is, c in vacuum—the extracted electrons can co-move with the laser and be accelerated continually. In doing so, these extracted electrons gain transverse energy from the laser's E_y field, and this transverse momentum is converted into forward momentum by the $\mathbf{v} \times \mathbf{B}$ term of the Lorentz force. The larger-than-c phase velocity in the curved portion of the cone wall reduces both the electron trapping efficiency and the acceleration time before dephasing, whereas in the near-grazing incidence, $v_w \to c$.

Unlike the previous laser-cone interaction model[49] involving microfocusing of the laser light, and resulting in electron guiding along the cone walls down to the cone tip, in the model presented here, the laser grazes along the cone wall and the electron acceleration takes place in the laser direction. For an increasing acceleration length, the continuous loading of electrons into the accelerating phase of the laser field yields an increase in high-energy electrons. Increasing the length between the curved cone and the top should further increase proton energies, provided the laser field is still sufficiently strong. This was tested in the simulations by adding a portion of straight length between the curved cone and the flat top to increase the acceleration length ℓ, which, as illustrated in Fig. 14(a), corresponds to the distance along the cone wall, projected onto the laser axis, between the flat top and the point where the laser axis is 1 μm away from the cone wall. In Fig. 14(b), we indeed find that the temperature of the electrons increases with ℓ,

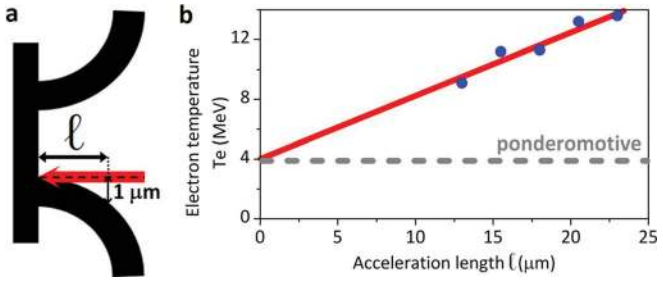

FIG. 14. (Color) (a) Acceleration length ℓ; (b) PICLS simulations at t = 900 fs: Electron temperature (for electrons within the [20 MeV; 40 MeV] energy range) as a function of ℓ, compared to the ponderomotive temperature (horizontal gray dashed line).

and can thus become considerably larger than that of the ponderomotively heated electrons.

V. CONCLUSIONS AND FUTURE OUTLOOK

In scalings, regarding proton energy as a function of laser intensity,[29,30,65] reporting on laser interactions with flat-foil targets, it is inferred that increasing the laser energy is necessary to get to therapeutic proton energies, and especially to the upper-end of the therapeutic window. The model in Ref. 65, depending on the parameters used (e.g., electron divergence and temperature) predicts >100 MeV for flat-foil targets, using the Trident laser parameters. However—experimentally—only 50 MeV are measured, while the PICLS simulations yield 44 MeV for a RMT.

In the experiments described here, since the laser spot size is small and the contrast very high, a central alignment of the laser into the FTC yields similar results as an RMT. However, we observe a clear increase in proton energy, up to 67.5 MeV, for a wide-neck FTC target where the laser grazed along the cone wall and interacted with the flat top. Because of the asymmetry of the interaction, a new important understanding of a novel hot-electron generation mechanism was developed: to our knowledge, this DLLPA of surface-guided electrons has not been considered before to enhance the target normal sheath accelerated protons in cones.[49,50] The nongrazing geometry presented in Ref. 66 limits the length of the acceleration region that is determined by the laser focus diameter; while in our case, the acceleration takes place along the laser axis. As the laser and hot electrons both move at c, electrons are directly trapped in an accelerating laser phase, being confined inside the laser focus by the self-generated surface potential. In Ref. 49, electrons could not be preaccelerated to sufficient energies to be trapped in the laser accelerating phase, possibly because the laser intensity was lower (4×10^{18} W/cm^2 vs 2×10^{20} W/cm^2) and the cone geometry was different (straight cone vs curved cone wall). In Ref. 50, no x-ray imaging was available to observe the laser–cone interaction, thus, no correlation between the highest proton energies and laser grazing along the cone wall could be found in that work.

Both the experimentally observed >60 MeV proton energies as well as our 2D PIC simulations suggest that, for laser intensities of 1.5×10^{20} W/cm^2, the higher proton energies obtained in the asymmetrically irradiated FTC result from the DLLPA of the electrons along the interior surface of the cone wall, while the effect of laser-guiding of the cone is of lesser importance.

Future experiments will require more stable laser alignment and pointing to achieve a higher level of control in laser grazing and polarization of the laser–wall interaction, and possibly achieve even higher proton energies. In addition, it will be useful to use two orthogonal x-ray imagers to determine the laser–wall polarization, as well as a Bremsstrahlung spectrometer to characterize the electron energy distribution inside the cone walls, and to optimize it with respect to target geometry and laser pointing and polarization. Our new physical understanding will enable further target development of optimized target shapes, e.g., extension of the acceleration length ℓ; and of simpler targets. If the results obtained here at ~80 J and $\sim 1.5 \times 10^{20}$ W/cm^2 became achievable at ~10 J and similar intensities on a high-repetition-rated laser system, it would open the door to a variety of applications, and in particular to laser-based hadron-therapy.

ACKNOWLEDGMENTS

The authors would like to express their gratitude to the Trident laser crew and director: F. L. Archuleta, R. P. Gonzales, T. R. Hurry, R. P. Johnson, S.-M. L. Reid, T. Shimada; and D. S. Montgomery. The authors would also like to thank J. S. Cowan for scanning the RCFs on a MicroD, D. C. Gautier for help setting up the experiment, J. Workman for the loan of the imaging crystal, Nanolabz (especially G. Korgan and S. Malekos) for targets, J. Baas for help mounting targets, B. Montoya and J. Velarde for machining parts, E. d'Humières for help setting up the simulations, and R. Presura for useful comments. T.E.C. would like to thank S. D. Kraft, U. Schramm, and K. Zeil for useful discussions. K.A.F, D.T.O., and B.G. would like to thank the LANL LDRD program for supporting Trident, financing the targets, and the experiments performed at LANL. M.S. and M.G. were supported by Sandia National Laboratories, under DOE-NNSA contract number DE-AC04-94AL85000. The simulation work was partially supported by JSC computing grant HDR04 and onCOOPtics grant 03ZIK445.

[1]M. Dunne, Science **312**, (5772), 374 (2006).
[2]R. Snavely, M. Key, S. Hatchett, T. Cowan, M. Roth, T. Phillips, M. Stoyer, E. Henry, T. Sangser, M. Signh, S. Wilks, A. Mackinnon, A. Offenberger, D. Pennington, K. Yasuike, A. Langdon, B. Lasinski, J. Johnson, M. Perry, and E. Campbell, Phys. Rev. Lett. **85**, 2945 (2000); S. P. Hatchett, C. G. Brown, T. E. Cowan, E. A. Henry, J. S. Johnson, M. H. Key, J. A. Koch, A. B. Langdon, B. F. Lasinski, R. W. Lee, A. J. Mackinnon, D. M. Pennington, M. D. Perry, T. W. Phillips, M. Roth, T. C. Sangster, M. S. Singh, R. A. Snavely, M. A. Stoyer, S. C. Wilks, and K. Yasuike, Phys. Plasmas **7**, 2076 (2000).
[3]A. Maksimchuk, S. Gu, K. Flippo, and D. Umstadter, Phys. Rev. Lett. **84**, 4108 (2000).
[4]E. L. Clark, K. Krushelnick, J. R. Davies, M. Zepf, M. Tatarakis, F. Beg, A. Machacek, P. A. Norreys, M. I. K. Santala, I. Watts, and A. E. Dangor, Phys. Rev. Lett. **84**, 670 (2000).
[5]S. A. Gaillard, J. Fuchs, N. Renard-Le Galloudec, and T. E. Cowan, Phys. Rev. Lett. **96**, 249201 (2006).
[6]B. A. Remington, R. P. Drake, and D. D. Ryutov, Rev. Mod. Phys. **78**, 755 (2006).

[7]K. W. D. Ledingham, P. McKenna, and R. P. Singhal, Science **300**, 1107 (2003).
[8]K. Nemoto, A. Maksimchuk, S. Banerjee, K. Flippo, G. Mourou, D. Umstadter, and V. Y. Bychenkov, Appl. Phys. Lett. **78**, 595 (2001).
[9]M. Roth, T. Cowan, M. Key, S. Hatchett, C. Brown, W. Fountain, J. Johnson, D. Pennington, R. Snavely, S. Wilks, K. Yasuike, H. Ruhl, F. Pegoraro, S. Bulanov, E. Campbell, M. D. Perry, and H. Powell, Phys. Rev. Lett. **86**, 436 (2001).
[10]B. A. Hammel, C. J. Keane, M. D. Cable, D. R. Kania, J. D. Kilkenny, R. W. Lee, and R. Pasha, Phys. Rev. Lett. **70**, 1263 (1993).
[11]R. L. Kauffman, L. J. Suter, C. B. Darrow, J. D. Kilkenny, H. N. Kornblum, D. S. Montgomery, D. W. Phillion, M. D. Rosen, A. R. Theissen, R. J. Wallace, and F. Ze, Phys. Rev. Lett. **73**, 2320 (1994).
[12]P. Y. Chang, R. Betti, B. K. Spears, K. S. Anderson, J. Edwards, M. Fatenejad, J. D. Lindl, R. L. McCrory, R. Nora, and D. Shvarts, Phys. Rev. Lett. **104**, 135002 (2010).
[13]V. A. Smalyuk, R. Betti, J. A. Delettrez, V. Yu. Glebov, D. D. Meyerhofer, P. B. Radha, S. P. Regan, T. C. Sangster, J. Sanz, W. Seka, C. Stoeckl, B. Yaakobi, J. A. Frenje, C. K. Li, R. D. Petrasso, and F. H. Séguin, Phys. Rev. Lett. **104**, 165002 (2010).
[14]M. Borghesi, D. H. Campbell, A. Schiavi, M. G. Haines, O. Willi, A. J. MacKinnon, P. Patel, L. A. Gizzi, M. Galimberti, R. J. Clarke, F. Pegoraro, H. Ruhl, and S. Bulanov, Phys. Plasmas **9**, 2214 (2002).
[15]L. Romagnani, J. Fuchs, M. Borghesi, P. Antici, P. Audebert, F. Ceccherini, T. Cowan, T. Grismayer, S. Kar1, A. Macchi, P. Mora, G. Pretzler, A. Schiavi, T. Toncian, and O. Willi, Phys. Rev. Lett. **95**, 195001 (2005).
[16]T. E. Cowan, J. Fuchs, H. Ruhl, A. Kemp, P. Audebert, M. Roth, R. Stephens, I. Barton, A. Blažević, E. Brambrink, J. Cobble, J. Fernandez, J.-C. Gauthier, M. Geissel, M. Hegelich, J. Kaæ, S. Karsch, G. P. Le Sage, S. Letzring, M. Manclossi, S. Meyroneinc, A. Newkirk, H. Pepin, and N. Renard-Le Galloudec, Phys. Rev. Lett. **92**, 204801 (2004).
[17]K. Krushelnick, E. L. Clark, R. Allott, F. N. Beg, C. N. Danson, A. Machacek, V. Malka, Z. Najmudin, D. Neely, P. A. Norreys, M. R. Salvati, M. I. K. Santala, M. Tatarakis, I. Watts, M. Zepf, A. E. Dangor, IEEE Trans. Plasma Sci. **28**, 1184 (2000).
[18]P. Antici, M. Fazi, A. Lombardi, M. Migliorati, L. Palumbo, P. Audebert, and J. Fuchs, J. App. Phys. **104**, 124901 (2008).
[19]U. Linz and J. Alonso, Phys. Rev. ST—Accel. Beams **10**, 094801 (2007).
[20]K. W. D. Ledingham, W. Galster, and R. Sauerbrey, Br. J. Radiol. **80**, 855 (2007).
[21]J. Weichsel, T Fuchs, E Lefebvre, E d'Humières, and U Oelfke, Phys. Med. Biol. **53**, 4383 (2008).
[22]S. Schell and J. J. Wilkens, Phys. Med. Biol. **54**, N459 (2009).
[23]T. Toncian, M. Borghesi, J. Fuchs, E. d'Humières, P. Antici, P. Audebert, E. Brambrink, C. A. Cecchetti, A. Pipahl, L. Romagnani, and O. Willi, Science **312**, (2006).
[24]H. Schwoerer, S. Pfotenhauer, O. Jäckel, K.-U. Amthor, B. Liesfeld, W. Ziegler, R. Sauerbrey, K. W. D. Ledingham, and T. Esirkepov, Nature **439**, 445 (2006).
[25]E. Fourkal, J. S. Li, W. Xiong, A. Nahum, and C.-M. Ma, Phys. Med. Biol. **48**, 3977 (2003).
[26]T. Zh. Esirkepov, S. V. Bulanov, K. Nishihara, T. Tajima, F. Pegoraro, V. S. Khoroshkov, K. Mima, H. Daido, Y. Kato, Y. Kitagawa, K. Nagai, and S. Sakabe, Phys. Rev. Lett. **89**, 175003 (2002).
[27]A. P. L Robinson and P. Gibbon, Phys. Rev. E **75**, 015401(R) (2007).
[28]S. A. Gaillard, K. A. Flippo, M. E. Lowenstern, J. E. Mucino, J. M. Rassuchine, D. C. Gautier, J. Workman, and T. E. Cowan, J. Phys.: Conf. Ser. **244**, 022034 (2010).
[29]K. Flippo, T. Bartal, F. Beg, S. Chawla, J. Cobble, S. A. Gaillard, D. Hey, A. MacKinnon, A. MacPhee, P. Nilson, D. T. Offermann, S. Le Pape, and M. J. Schmitt, J. Phys.: Conf. Ser. **244**, 022033 (2010).
[30]L. Robson, P.T. Simpson, R.J. Clarke, K. W. D. Ledingham, F. Lindau, O. Lundh, T. McCanny, P. Mora, D. Neely, C.-G. Wahlstrom, M. Zepf, and P. McKenna, Nat. Phys. **3**, 58 (2007).
[31]V. P. Cosgrove, A. C. A. Aro, S. Green, M. C. Scott, G. C. Taylor, D. E. Bonnett, and A. Kacperek, Rad. Prot. Dos. **44**, 405 (1992).
[32]T. Esirkepov, M. Borghesi, S. V. Bulanov, G. Mourou, and T. Tajima, Phys. Rev. Lett. **92**, 175003 (2004).
[33]T. Schlegel, N. Naumova, V. T. Tikhonchuk, C. Labaune, I. V. Sokolov, and G. Mourou, Phys. Plasmas **16**, 083103 (2009).
[34]A. P. L. Robinson, M. Zepf, S. Kar, R. G. Evans, and C. Bellei, New J. Phys. **10**, 013021 (2008).
[35]A. Macchi, S. Veghini, T. V. Liseykina, and F. Pegoraro, New J. Phys. **12**, 045013 (2010).
[36]K. Flippo, B. M. Hegelich, B. J. Albright, L. Yin, D. C. Gautier, S. Letzring, M. Schollmeier, J. Schreiber, R. Schulze, and J. C. Fernandez, Laser Part. Beams **25**, 3 (2007).
[37]L. Yin, B. J. Albright, B. M. Hegelich, K. J. Bowers, K. A. Flippo, T. J. T. Kwan, and J. C. Fernandez, Phys. Plasmas **14**, 056706 (2007).
[38]S. Wilks, A. Langdon, T. Cowan, M. Roth, M. Singh, S. Hatchett, M. Key, D. Pennington, A. MacKinnon, and R. Snavely, Phys. Plasmas **8**, 542 (2001).
[39]P. Mora, Phys. Rev. Lett. **90**, 185002 (2003).
[40]P. Mora, Phys. Rev. E **72**, 056401 (2005).
[41]S. D. Baton, M. Koenig, P. Guillou, B. Loupias, A. Benuzzi-Mounaix, Julien Fuchs, C. Rousseaux, L. Gremillet, D. Batani, A. Morace, M. Nakatsutsumi, R. Kodama and Y. Aglitskiy, High Energy Density Phys. **3**, 358 (2007).
[42]F. Perez, L. Gremillet, M. Koenig, S. D. Baton, P. Audebert, M. Chahid, C. Rousseaux, M. Drouin, E. Lefebvre, T. Vinci, J. Rassuchine, T. Cowan, S. A. Gaillard, K. A. Flippo, and R. Shepherd, Phys. Rev. Lett. **104**, 085001 (2010).
[43]S. Buffechoux, J. Psikal, M. Nakatsutsumi, L. Romagnani, A. Andreev, K. Zeil, M. Amin, P. Antici, T. Burris-Mog, A. Compant-La-Fontaine, E. d'Humières, S. Fourmaux, S. Gaillard, F. Gobet, F. Hannachi, S. Kraft, A. Mancic, C. Plaisir, G. Sarri, M. Tarisien, T. Toncian, U. Schramm, M. Tampo, P. Audebert1, O. Willi, T. E. Cowan, H. Pépin, V. Tikhonchuk, M. Borghesi, and J. Fuchs, Phys. Rev. Lett. **105**, 015005 (2010).
[44]T. Kluge, W. Enghardt, S. D. Kraft, U. Schramm, Y. Sentoku, K. Zeil, T. E. Cowan, R. Sauerbrey, and M. Bussmann, Phys. Rev. E **82**, 016405 (2010).
[45]C.-K. Huang, B. J. Albright, L. Yin, H.-C. Wu, K. J. Bowers, B. M. Hegelich, and J. C. Fernández, Phys. Rev. ST Accel. Beams **14**, 031301 (2011).
[46]R. Kodama, Y. Sentoku, Z. L. Chen, G. R. Kumar, S. P. Hatchett, Y. Toyama, T. E. Cowan, R. R. Freeman, J. Fuchs, Y. Izawa, M. H. Key, Y. Kitagawa, K. Kondo, T. Matsuoka, H. Nakamura, M. Nakatsutsumi, P. A. Norreys, T. Norimatsu, R. A. Snavely, R. B. Stephens, M. Tampo, K. A. Tanaka, and T. Yabuuchi, Nature **432**, 1005 (2004).
[47]J. S. Green, K. L. Lancaster, K. U. Akli, C. D. Gregory, F. N. Beg, S. N. Chen, D. Clark, R. R. Freeman, S. Hawkes, C. Hernandez-Gomez, H. Habara, R. Heathcote, D. S. Hey, K. Highbarger, M. H. Key, R. Kodama, K. Krushelnick, I. Musgrave, H. Nakamura, M. Nakatsutsumi, N. Patel, R. Stephens, M. Storm, M. Tampo, W. Theobald, L. Van Woerkom, R. L. Weber, M. S. Wei, N. C. Woolsey, and P. A. Norreys, Nat. Phys. **3**, 853 (2007).
[48]H. Nakamura, B. Chrisman, T. Tanimoto, M. Borghesi, K. Kondo, M. Nakatsutsumi, T. Norimatsu, M. Tampo, K. A. Tanaka, T. Yabuuchi, Y. Sentoku, and R. Kodama, Phys. Rev. Lett. **102**, 045009 (2009).
[49]Y. Sentoku, K. Mima, H. Ruhl, Y. Toyama, R. Kodama, and T. E. Cowan, Phys. Plasmas **11**, 3083 (2004).
[50]K. A. Flippo, E. d'Humières, S. A. Gaillard, J. Rassuchine, D. C. Gautier, M. Schollmeier, F. Nurnberg, J. L. Kline, J. Adams, B. Albright, M. Bakeman, K. Harres, R. P. Johnson, G. Korgan, S. Letzring, S. Malekos, N. Renard-Le Galloudec, Y. Sentoku, T. Shimada, M. Roth, T. E. Cowan, J. C. Fernandez, and B. M. Hegelich, Phys. Plasmas **15**, 5 (2008).
[51]K. A. Flippo, J. Workman, D. C. Gautier, R. P. Johnson, and T. Shimada, Rev. Sci. Instrum. **79**, 10E534 (2008).
[52]J. Rassuchine, E. d'Humières, S. D. Baton, P. Guillou, M. Koenig, M. Chahid, F. Perez, J. Fuchs, P. Audebert, R. Kodama, M. Nakatsutsumi, N. Ozaki, D. Batani, A. Morace, R. Redaelli, L. Grémillet, C. Rousseaux, F. Dorchies, C. Fourment, J. J. Santos, J. Adams, G. Korgan, S. Malekos, S. B. Hansen, R. Shepherd, K. Flippo, S. Gaillard, Y. Sentoku, and T. E. Cowan, Phys. Rev. E **79**, 036408 (2009). S. D. Baton, M. Koenig, J. Fuchs, A. Benuzzi-Mounaix, B. Loupias, T. Vinci, L. Grémillet, C. Rousseaux, M. Drouin, E. Lefebvre, F. Dorchies, C. Fourment, J. J. Santos, D. Batani, A. Morace, R. Redaelli, M. Nakatsutsumi, R. Kodama, A. Nishida, N. Ozaki, T. Norimatsu, Y. Aglitskiy, S. Atzeni, and A. Schiavi, Phys. Plasmas **15**, 042706 (2008).
[53]R. C. Shah, R. P. Johnson, T. Shimada, K. A. Flippo, J. C. Fernandez, and B. M. Hegelich, Optics Express **34**, 2273 (2008).
[54]D. Strickland and G. Mourou, Opt. Commun. **56**, 219 (1985).
[55]D. C. Gautier, K. A. Flippo, S. A. Letzring, J. Workman, T. Shimada, R. P. Johnson, T. R. Hurry, S. A. Gaillard, and B. M. Hegelich, Rev. Sci. Instrum. **79**, 10F547 (2008).
[56]R. P. Johnson, T. Shimada, and R. C. Shah, Techniques for Pre-pulse Contrast Improvement on the 0.5 ps, 80 J, "C" Beamline of the Trident Laser, Conference on Lasers and Electro-Optics Proceedings (submitted).

[57]J. A. Koch, Y. Aglitskiy, C. Brown, T. Cowan, R. Freeman, S. Hatchett, G. Holland, M. Key, A. Mackinnon, J. Seely, R. Snavely, and R. Stephens, Rev. Sci. Instrum. **74**, 2130 (2003).
[58]See http://www.fujifilm.com/products/life_science/si_imgplate/img_plate.html for Imaging Plates supplied by Fujifilm.
[59]See www.gafchromic.com for Gafchromic RCF type MD-V2-55 and HD-810, supplied by International Specialty Products www.gafchromic.com
[60]F. Nürnberg, M. Schollmeier, K. Harres, A. Blažević, P. Audebert, E. Brambrink, D. C. Carroll, K. Flippo, D. C. Gautier, B. M. Hegelich, O. Lundh, K. Markey, P. McKenna, D. Neely, and M. Roth, Rev. Sci. Instrum. **80**, 033301 (2007).
[61]Y. Sentoku and A. J. Kemp, J. Comp. Phys. **227**, 6846 (2008).
[62]R. B. Campbell, J. S. DeGroot, T. A. Mehlhorn, D. R. Welch, and B. V. Oliver, Phys. Plasmas **10**, 4169 (2003).
[63]A. P. L. Robinson and M. Sherlock, Phys. Plasmas **14**, 083105 (2007).
[64]Y. Sentoku and M. C. Downer, High Energy Density Phys. **6**, 268 (2010).
[65]J. Fuchs, P. Antici, E. d'Humières, E. Lefebvre, M. Borghesi, E. Brambrink, C. Cecchetti, M. Kaluza, V. Malka, M. Manclossi, S. Meyroneinc, P. Mora, J. Schreiber, T. Toncian, H. Pepin, and P. Audebert, Nature **2**, 48 (2006).
[66]T. Nakamura, K. Mima, H. Sakagami, and T. Johzaki, Phys. Plasmas **14**, 053112 (2007).